


*Interfacial fracture toughness measurement  
in both steady state and transient regimes  
using four-point bending test*

**M. E. M. Zebar, M. L. Hattali &  
N. Mesrati**



# Interfacial fracture toughness measurement in both steady state and transient regimes using four-point bending test

M. E. M. Zebar · M. L. Hattali  · N. Mesrati

Received: 24 July 2019 / Accepted: 4 February 2020  
© Springer Nature B.V. 2020

**Abstract** The paper describes some extensions of four-point bending tests for determining the interfacial fracture toughness  $\Gamma$ , in both steady-state and transient regimes, as a function of the fracture mode mixity. Two sets of multimaterial systems were studied: (i) Aluminum alloy (ASTM 2017)/epoxy/PMMA polymer and, (ii) Aluminum alloy (ASTM 2017)/stainless steel (ASTM 301) obtained by bonding and thermal spray coating techniques respectively. The interfacial fracture toughness was investigated by means of analytical and Finite Element Analysis using ABAQUS software. The numerical trend solution of both interfacial fracture toughnesses as function of crack length, and friction coefficient has been obtained and compared to an analytical one. We will propose a method on (i) how both reversed notch position in multimaterial systems and crack delamination beyond the inner loading points (transient regime) are explored to extend the measurement of interfacial fracture toughness, (ii) how the numerical analysis is used to determine the

interfacial fracture toughness through an experimental compliance measurement in transient regime, and (iii) we attempt to reveal why the interfacial toughness has strong phase angle dependence.

**Keywords** Delamination · Interfacial fracture energy · Four-point bending · Mixed mode

## 1 Introduction

Fracture at interfaces between dissimilar materials have attracted significant attention from scientists and engineers and is a critical phenomenon in many systems, ranging from natural to artificial products. Examples include skin and tissue in biological bodies, micro-electronic devices, debonding of fiber in composites and decohesion of thin film coatings or thermal barrier coatings in engineering structures, among many others (Clarke and Levi 2003; Gan et al. 2005; Hattali et al. 2009, 2010, 2012; Ranjbar-Far et al. 2012; Yang et al. 2015; Richards et al. 2016). These layered structures undergo complex failure modes, often related to interface cracking. Therefore, to design reliable layered structures, it is paramount that the mechanics of the interface crack are understood. The need to understand, quantify and improve the toughness of advanced materials has renewed interest in the elastic interface crack problem and has received attention through analytical (e.g., see Cherepanov 1979; Hutchinson and Suo 1992; Begley and Hutchinson 2017), experimen-

---

M. E. M. Zebar  
Laboratoire de Génie mécanique et développement, École  
Nationale Polytechnique d'Alger, El Harrach, Algeria  
e-mail: mohamed\_el\_mahdi.zebar@g.enp.edu.dz

M. L. Hattali (✉)  
Université Paris-Saclay, CNRS, FAST, 91405 Orsay,  
France  
e-mail: lamine.hattali@universite-paris-saclay.fr

N. Mesrati  
Laboratoire de Sciences et Génie des Matériaux, École  
Nationale Polytechnique d'Alger, El Harrach, Algeria  
e-mail: nadir.mesrati@g.enp.edu.dz

tal (e.g., Charalambides et al. 1989; Wang and Suo 1990; Yuuki et al. 1994; Ikeda et al. 1998; Swadener et al. 1999; Begley and Hutchinson 2017) and numerical simulations (e.g., see Matos et al. 1989; Toya 1992; Yang et al. 2015). Contrary to homogeneous, isotropic materials, where cracks tend to propagate in pure mode I locally at the crack tip, the interface fracture problems involve combinations of normal and shear displacements along the crack, such that “mixed mode I + II” conditions prevail. For a bimaterial interface crack, mode mixity is not as clearly defined as it is for isotropic materials, due to the oscillatory solution obtained near the crack tip. A measure of the mode mixity, sometimes called the phase angle,  $\psi$ , is equal to the stress ratio  $\sigma_{12}/\sigma_{22}$  at  $r = l$  on the interface ahead of the crack tip and defined as follows,

$$\psi = \tan^{-1} \left[ \left( \frac{\sigma_{12}}{\sigma_{22}} \right)_{r=l} \right] = \tan^{-1} \left[ \left( \frac{\text{Im}[Kl^{i\epsilon}]}{\text{Re}[Kl^{i\epsilon}]} \right) \right] \quad (1)$$

Thus, this measure depends on the choice of reference length  $l$ . The latter describes the location where the mode mixity is evaluated ahead of the crack tip. There are no fixed guidelines on how to select the reference length. A mode mixity based on a material-scale reference length  $l$  is adopted by some authors (Rice 1988; Hutchinson and Suo 1992; Odowd et al. 1992; Ikeda et al. 1998). It is usually based either on the specimen geometry (crack length or layer thickness) (Yuuki et al. 1994), a material scale (grain size, the plastic zone or fracture process zone) (Rice 1988; Rice et al. 1990; Hutchinson and Suo 1992) or by judgement (Dollhofer et al. 2000). It is readily shown that local phase angles  $\psi_1$  and  $\psi_2$  associated with two different reference lengths  $l_1$  and  $l_2$  are related by equation:

$$\psi_2 = \psi_1 + \epsilon \ln \left( \frac{l_2}{l_1} \right) \quad (2)$$

Hence, the local phase angle shift between two choices of  $l$  in an interval of physically relevant scales may be negligible when  $\epsilon$  is sufficiently small. The phase angle depends on the loading geometry, relative layer thickness and relative elastic properties of the two materials. There is a lot of experimental works which show that interfacial fracture toughness depends strongly on the mode mixity (Wang and Suo 1990; Evans et al. 1990; Yuuki et al. 1994; Wu et al. 2016). The fracture resistance of the interface can be quantified by an energy, the interfacial fracture toughness  $\Gamma$ .

The contributions to  $\Gamma$  come from the work of adhesion and the dissipative work. The latter (e.g., plasticity, roughness, and shielding effects of the interface) increases with mode II loading and can be significantly larger than the work of adhesion (Evans et al. 1990; Dauskardt et al. 1998). It was noticed that the interfacial fracture toughness increased as the mode II contribution increased. Thus,  $\Gamma$  is governed by the mode mixity, which relates the relative proportions of the sliding to the opening modes ahead of the crack tip (Evans et al. 1990). It could be mainly associated with the contact shielding effect due to the initial roughness of the interface (Evans and Hutchinson 1989). Liechti and Chai (1992) studied a glass/epoxy interface and measured the interfacial toughness over a wide range of mode mixity. It was found that a toughening effect was associated with increasing positive and negative in-plane shear components. They suggest that the inelastic behavior (bulk viscoelastic dissipation and viscoplasticity) of the epoxy, frictional, and, perhaps, three-dimensional effects should be considered. The interfacial fracture is characterized by a toughness curve, expressing the interfacial fracture toughness as a function of mode mixity. The toughness curve is a property of the bimaterial interface and should be invariant of the specimen type or specimen geometry.

The purpose of the work presented here is to examine interfacial fracture toughness,  $\Gamma$ , as a function of the fracture mode mixity. We present the results and analysis of a series of experiments that were conducted on two dissimilar materials loaded in four-point bending tests. The first one consists of thermal spray wire austenitic stainless steel (ASTM 301) coatings on flame sprayed aluminum alloy (ASTM 2017) substrates and is produced by means of Electric Arc spray 234. Thanks to their mechanical and chemical properties, stainless steels ASTM 301 are relevant to tribological, wear and corrosion resistance in different environments (Zeng et al. 2006; Sadki et al. 2016). The second one consists to bond PMMA to aluminum alloy (ASTM 2017) as a model material, by using epoxy resin. The numerical calculations are carried out by the Finite Element Analysis using Abaqus software. The numerical trend solution of both interfacial fracture toughnesses as function of crack length, and friction coefficient has been obtained and compared to an analytical one. On loading in four-point bending tests, interface cracks grow on both sides of the notch at the critical fracture load. The specimen has an advantageous configuration such

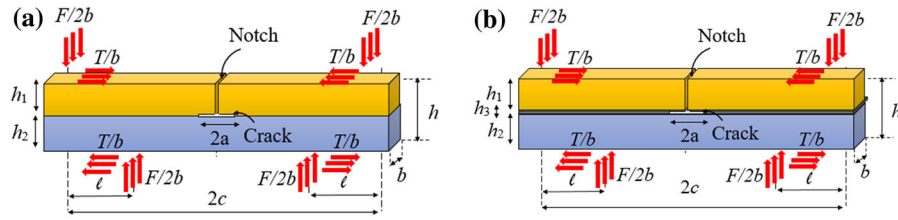


**Fig. 1** Geometry and nomenclature of the loading conditions for the notched four-point bending specimen with symmetrical interfacial cracks. **a** Bimaterial system, **b** multimaterial system. Where  $F$  and  $T$  denotes the applied and tangential forces

that when the interface crack extends a few times the thickness of the top layer but still lying within the central region of the specimen, it can be considered as semi-infinite, undergoing steady-state propagation (Charalambides et al. 1989). Between the inner loading points, the bending moment is constant. Thus, the mode mixity remains constant as the crack propagates and it is not necessary to monitor the crack length accurately. In this configuration, the analytical solution is used to calculate the interfacial fracture toughness. However, when crack length,  $a$ , is much larger than the deposit film,  $h_1$ , or when the crack goes beyond the inner loading points the tested specimen does not fulfill the geometrical condition for a steady-state region (see Fig. 1). Thus, the mode mixity increases. In this situation, the use of the compliance method is unavoidable which is based on finite element analysis and was conducted in two steps:

- i. By knowing the measured compliance, the crack length is first determined from numerical compliance versus crack length curve;
- ii. Then, by knowing the crack length, the energy release rate of the interface  $G_c$  (equal to the toughness of the interface  $\Gamma$ ) can be determined from numerical energy release rate versus crack length curve.

The results show that the interfacial fracture toughness increases with loading phase angle. We discuss this tendency by analyzing interfacial crack path and crack surface.

## 2 Experimental measurements and analysis

### 2.1 Specimens and experimental set-up

We investigate the interfacial fracture toughness of two sets of multimaterials systems using four-point flex-

**Table 1** Thermal spray conditions

| Parameter                        | Value     |
|----------------------------------|-----------|
| Air pressure in the engine       | 3.8 bars  |
| Air pressure in the spray nozzle | 3 bars    |
| Speed of wire moving             | 0.064 m/s |
| Generator voltage                | 30 V      |
| Current intensity                | 100 A     |
| Spraying distance                | 140 mm    |
| Firing angle                     | 90°       |
| Wire diameter                    | 1.6 mm    |

ure specimens: specimen A and specimen B. Specimen A consists of thermal spray wire stainless steel (ASTM 301) coatings on flame sprayed aluminum alloy (ASTM 2017) substrates and were produced by means of Electric Arc spray 234 (Metal Spary Co., Ltd, Auckland, New Zealand). The four-point bending test has been used extensively for interfacial testing of bimaterial interfaces, composite laminates, metallic adhesive joints, and thin films (Charalambides et al. 1989; Suo and Hutchinson 1990; Hutchinson and Suo 1992; Becker et al. 1997; Dauskardt et al. 1998). It contains a notch in the center of the top layer, which reaches the interface (Fig. 1). Prior to bonding, the surface of aluminum alloy (ASTM 2017) is sandblasted to increase the adhesion and then cleaned with acetone. Table 1 presents all the important thermal spray parameters used. Specimen B has PMMA polymer (Altuglas®) as the top layer, bonding with epoxy resin (Epoxy UHU plus endfest 300) on aluminum alloy (ASTM 2017).

The thickness of the top layer is  $h_1$ , and that of the bottom layer and intermediate layer are  $h_2$  and  $h_3$ . Thus, the total thickness of specimen is  $h = h_1 + h_2 + h_3$ . The length and width of all the spec-

**Table 2** Dimensions of the specimens

| Specimen no | $\alpha = \frac{E_2}{E_1}$ | $h_1$ (mm) | $h_2$ (mm) | $\eta = \frac{h_1}{h_2}$ | Number of sample |
|-------------|----------------------------|------------|------------|--------------------------|------------------|
| Specimen A  |                            |            |            |                          |                  |
| A1          | $\sim 0.33$                | 0.5        | 5          | 0.1                      | 5                |
| A2          | $\sim 0.33$                | 2          | 2          | 1                        | 5                |
| A3          | $\sim 3$                   | 1          | 10         | 0.1                      | 5                |
| A4          | $\sim 3$                   | 2          | 2          | 1                        | 5                |
| Specimen B  |                            |            |            |                          |                  |
| B1          | $\sim 25$                  | 1          | 10         | 0.1                      | 5                |
| B2          | $\sim 25$                  | 10         | 10         | 1                        | 5                |

**Table 3** Material properties

| Material                 | E (GPa) | $\nu$ |
|--------------------------|---------|-------|
| PMMA polymer Altuglas    | 2.75    | 0.38  |
| Epoxy                    | 2.03    | 0.37  |
| Aluminum ASTM 2017       | 70.1    | 0.35  |
| Stainless steel ASTM 301 | 210     | 0.29  |

imens are  $L = 100$  mm and  $b = 6$  mm respectively. The distance between the inner support pins and outer loading pins is 20 mm and 40 mm respectively (Fig. 1). Various combinations of  $h_1$  and  $h_2$  are considered for each set of specimens A and B, thus, to obtain various mixed mode (Suo and Hutchinson 1990; Hutchinson and Suo 1992) as shown in Table 2.

The mechanical properties of the materials are shown in Table 3. The modulus of elasticity  $E$  for PMMA polymer (Altuglas<sup>®</sup>) and aluminum alloy (ASTM 301) is determined from tension test. PMMA is a quasi-brittle material with linear-elastic behavior. The modulus of elasticity  $E$  and Poisson's ratio  $\nu$  for epoxy resin is based on the published data (Liechti and Chai 1992). The aluminum and stainless steel are assumed to respond linear elastically during the test. Poisson's ratio  $\nu$  of PMMA, ASTM 2017 and ASTM 301 are based on the published data (Comte and von Steub 2002; McGraw-Hill 2002).

## 2.2 Sample preparation

The two specimens A and B were prepared for mechanical testing. In specimen A1 and A2 ( $\alpha \sim 0.33$ ), the ASTM 301 is the notched top layer with ASTM 2017

as the intact bottom layer. The order is reversed in the case of sets A3 and A4 ( $\alpha = 3$ ) with the ASTM 2017 being the notched top layer and ASTM 301 as the intact bottom layer. In specimen B1 and B2 ( $\alpha \sim 25$ ) the PMMA is the notched top layer with ASTM 2017 as the intact bottom layer (see Table 2). The notch was made by a micro-mill (MDX500) running at high speed (12,000 rpm). The incorporation of an interfacial pre-crack is achieved by loading the notched section in three-point bend, such that the crack, once initiated, is subject to diminishing  $G$  and thus arrest. This procedure was designed to produce a short "T" shaped pre-crack (Fig. 2). During loading the force pre-crack of  $a = 4 \pm 1$  mm was observed.

## 2.3 Interfacial toughness testing

The bilayer specimens (A and B) were loaded in four-point bending mode using an electro-mechanical testing machine (Instron 5882) under displacement-controlled condition at a constant rate of 0.1 mm/min (Figs. 2 and 3). The friction between specimen and loading pins is measured by wear testing apparatus (Table 4).

To observe any crack initiation and propagation events, the set-up was placed under a digital microscope (Keyence). The displacement was measured by mean of gray scale correlation (ImageJ). Both the applied load and the displacement of the loading points were continuously monitored and recorded (Fig. 3a, b). The specimens were loaded until both cracks had propagated out to the inner loading points. The largest source of scatter in the fracture load is due to misalignment of the loading pins resulting in that the interfacial crack do not initiate simultaneously at the two sides of the notch. Therefore, the samples with more than 10% difference in the fracture load for crack initiation were discarded. One to five specimens are used for each combination of layer thicknesses,  $h_1$  and  $h_2$  for specimen sets A and B.

In Fig. 3b, a typical force-displacement curve is plotted. The load increased proportionally to displacement; in this stage (From 0 to (i)), no crack propagation occurs and the crack opening at the center is very small. Only in the case of A1 and A2 specimens and just before the identifier point (i), it looks like a significant damage development due to plastic deformation of ASTM 2017 substrate. No crack growth was observed. The

**Fig. 2** Schematic illustration of **a** the pre-cracking technique, with the specimen in the three point bending, and **b** the four point bend set-up

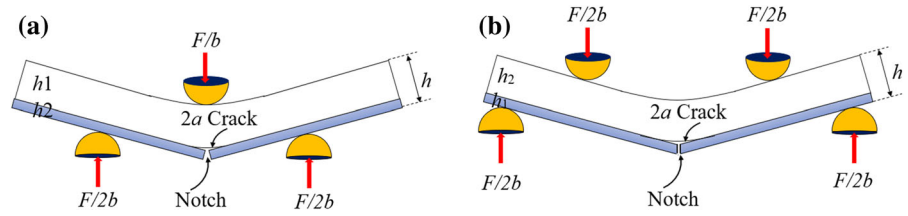


**Fig. 3 a** The four-point bend set-up. **b** Typical load–displacement curve in the four-point bending test for ASTM 2017A/ASTM 301 bimaterial (specimen A1). The slope of straight line is equivalent to the stiffness of the sample containing the pre-crack

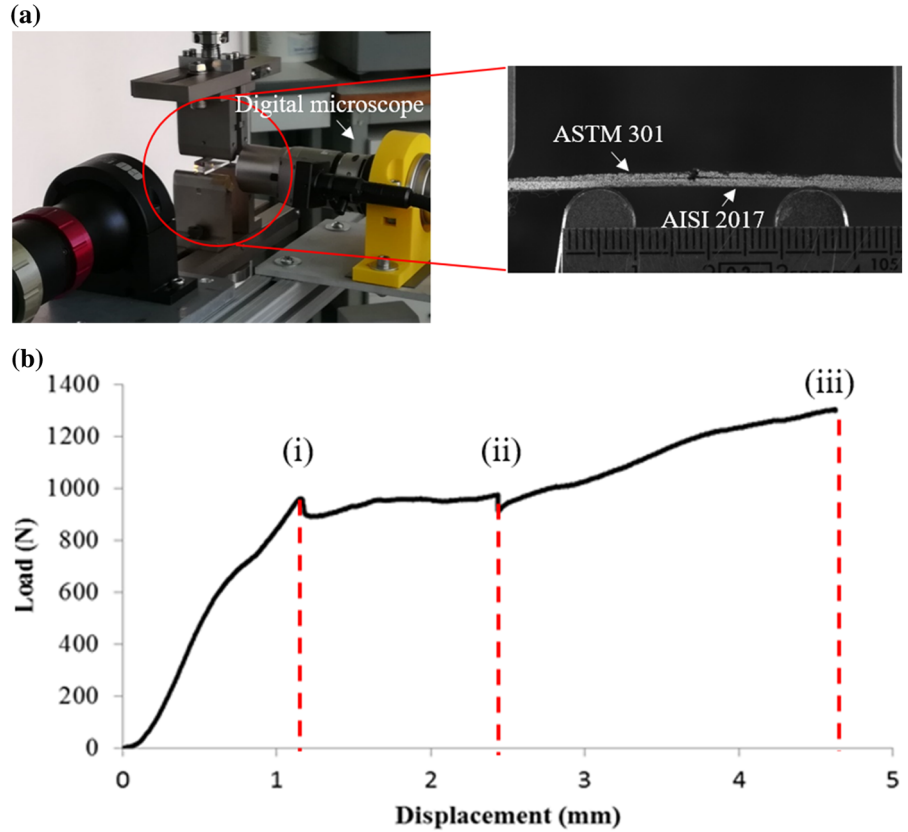


**Table 4** Friction properties: a test conditions:  $F = 10 \text{ N}$ ,  $V = 0.1 \text{ ms}^{-1}$ ,  $T = 22^\circ\text{C}$ , relative humidity range 12 to 55 %; laboratory air; sliding distance 1000 m, steel = ASTM 301, aluminum = ASTM 2017

|                      | Specimen pairs  |                |                |
|----------------------|-----------------|----------------|----------------|
|                      | Steel/steel     | Steel/aluminum | Steel/PMMA     |
| Friction coefficient | $0.51 \pm 0.11$ | $0.39 \pm 0.7$ | $0.32 \pm 0.6$ |
| Number of values     | 10              | 10             | 10             |

slope of the straight line is equivalent with the stiffness (reciprocal of the compliance) of the sample containing

the pre-crack. Deviation of the initial straight line corresponds to further crack propagation, where the load  $P$  reaches a critical value  $P_c$  at the given crack length. In this case the critical strain energy release rate does not vary significantly along the interface. Interfacial delamination along interface was observed to behave symmetrically until the crack tips approached the inner loading lines (From (i) to (ii)). For specimen A3, A4, B1 and B2, the interfacial fracture is irregular and shows the attributes of mode II in homogenous materials. For specimen A1 and A2, the interfacial fracture is similar to cleavage fracture associated with mode I in homogenous materials. In some cases, segmentation cracks and micro-cracks on the top of ASTM 301 coating was observed. This segmentation decreases the stored elas-

tic energy in the layer and makes the evaluation of the interface fracture energy difficult (Hofinger et al. 1998). The load again increases proportionally to the displacement. Compared to the first region, the compliance of the sample increases, due to the previous crack growth event (From (ii) to (iii)). In this case, the critical strain energy release rate, and therefore  $P_c$ , varies considerably with crack position. The (iii) point correspond to the ultimate strength of the aluminum alloys substrate.

## 2.4 Specimen analysis

In the case of steady-state condition and assuming no residual stresses, the total strain energy release rate can be determined analytically as the difference in the elastic strain energy in the cracked and uncracked parts of the four-point bending specimen (Fig. 1). Under the assumption of Hook's law, the steady-state energy release rate  $G_{ss}$  can then be calculated as a modification of Charalambides et al. (1989, 1990):

$$G_{ss} = \frac{M_b^2(1 - \nu_2^2)}{2E_2} \left( \frac{1}{I_2} - \frac{\lambda}{I_c} \right) \quad (3)$$

where  $I_2 = \frac{h_2^3}{12}$  and  $I_c = \frac{h_1^3}{12} + \lambda \frac{h_2^3}{12} + \lambda \frac{h_1 h_2 (h_1 + h_2)^2}{4(h_1 + \lambda h_2)}$  are the second moments of inertia per unit cross-sectional area for the bottom layer and the composite beam, respectively, and  $\lambda = \frac{E_2(1 - \nu_1^2)}{E_1(1 - \nu_2^2)}$ .

The strain energy release rate  $G_{ss}$  thus becomes:

$$G_{ss} = \frac{3 F^2 l^2 (1 - \nu_2^2)}{2 h^3 b^2 E_2} \left( \frac{1}{\left(\frac{h_2}{h}\right)^3} - \frac{\lambda}{\left(\left(\frac{h_1}{h}\right)^3 + \lambda \left(\frac{h_2}{h}\right)^3 + 3\lambda \left(\frac{h_1 h_2}{h^2}\right) \left(\frac{h_1}{h} + \lambda \frac{h_2}{h}\right)^{-1}\right)} \right) \quad (4)$$

It is also apparent that neglect of friction when it exists, would result in an overestimate of  $G_{ss}$ . The moment governed by applied and friction loads are:

$$M_b = M_b^F + M_b^{Friction} \quad (5)$$

where

$$M_b^F = \frac{Fl}{2b} \quad \text{and} \quad M_b^{Friction} = -\frac{Th}{b}$$

Consequently, for Colomb friction law:

$$M_b = \frac{Fl}{2b} \left( 1 - \mu \frac{h}{l} \right) \quad (6)$$

The steady state energy release rate becomes,

$$G_{ss} = \frac{3 F^2 l^2 (1 - \nu_2^2)}{2 h^3 b^2 E_2} \left( \frac{1}{\left(\frac{h_2}{h}\right)^3} - \frac{\lambda}{\left(\left(\frac{h_1}{h}\right)^3 + \lambda \left(\frac{h_2}{h}\right)^3 + 3\lambda \left(\frac{h_1 h_2}{h^2}\right) \left(\frac{h_1}{h} + \lambda \frac{h_2}{h}\right)^{-1}\right)} \right) \left( 1 - \mu \frac{h}{l} \right)^2 \quad (7)$$

At fracture load, the total strain energy release rate in Eq. (7) is denoted  $G_C$  and equals the interfacial toughness  $\Gamma$ . Now, when crack length,  $a$ , goes beyond the inner loading points (constant moment region). The use of a compliance method is unavoidable which is based on finite element analysis. The fracture parameters (the interfacial toughness  $\Gamma$  and the mode mixity  $\psi$ ) for the test specimens are determined based on finite element analysis. In this study, a model has been constructed for the bi-layers Aluminum alloy (ASTM 2017)/stainless steel (ASTM 301) and three-layers Aluminum alloy (ASTM 2017)/epoxy/PMMA polymer specimens. The analysis was performed using Abaqus 6.14 environment (Abaqus 2014), assuming a two-dimensional geometry. Because of the model symmetry, the finite element modelling can be restricted to half of the sample geometry. The finite element meshes of specimens which have aspect ratios height/out-of-plane width less than one ( $h/b < 1$ ) were constructed with eight-noded biquadratic plane strain elements (CPE8R). Whereas, for  $h/b > 1$  the finite element meshes were constructed with eight-noded biquadratic plane stress elements (CPS8R). For all cases, the crack tip elements were modelled with the appropriate stress singularity using collapsed eight-noded elements with the quarter-point mid-side node technique. The number of elements were varied with the relative thickness aspect ratio  $\eta$  and with the dimensionless crack length  $a/l$ . A focused mesh was used to discretize the near tip region (Fig. 4) and thus assure high accuracy. The near-tip mesh consists of 10 contours of elements meshed. The contact problem has been modeled as a deformable bi-material/three-material being pressed against cylinder, rigid surface. Therefore, two contact surfaces are required: one (the slave surface in Abaqus/Standard) on the deformable bi-material and the other (the master surface in Abaqus/Standard) on the rigid body. Abaqus assumes by default that the interaction between contacting bodies is frictionless. To define friction coefficients, we use the friction formulation option. Crack



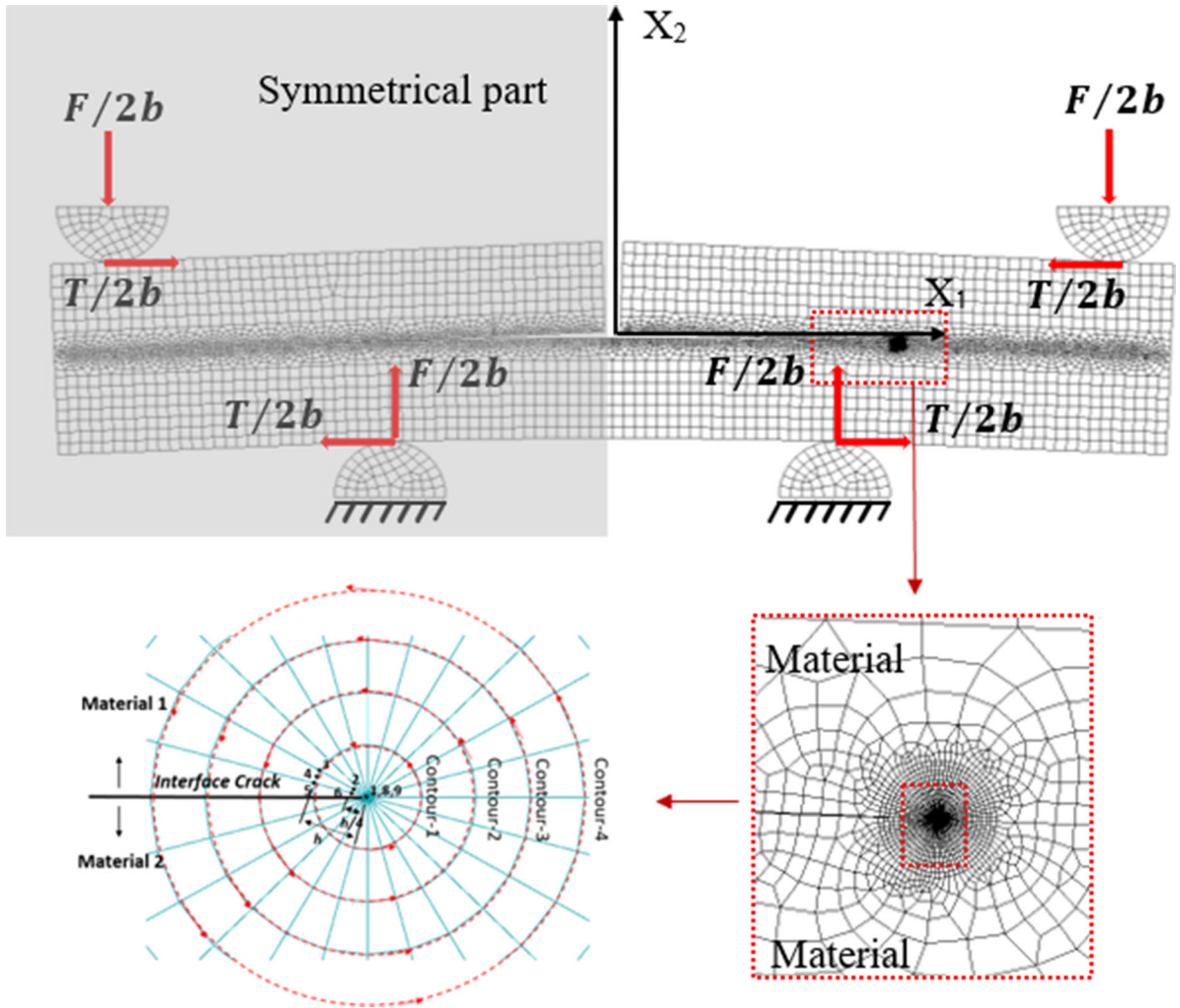


**Fig. 4** The mesh and the boundary conditions used in the finite element analysis; various contours for the calculation of the J-integral and stress intensity factors  $K_I$  and  $K_{II}$

edge contact or interpenetration was not observed. The deformed near-tip mesh clearly illustrates the relative opening and sliding crack face displacements that are indicative of mixed mode loading. The latter is computed from the values of the real and imaginary parts of the complex stress intensity factors,  $K_I$  and  $K_2$  (see Eq. (6)) (Rice and Sih 1965). These values are available directly from Abaqus.

$$K_I + iK_2 = Kl^{i\epsilon} = Ke^{i\psi} \quad (8)$$

where  $K$  is the complex stress intensity factor and has units of  $\text{Nm}^{-2}\sqrt{m} m^{i\epsilon}$ ,  $K_I$  and  $K_2$  are scale sensitive and change with the dimensional units and  $\psi$  is the mode mixity of  $Kl^{i\epsilon}$  (see Eq. (1)). It is important to

note that the phase angles reported for the considered multimaterial systems do not necessarily reflect relative sliding and opening of the crack surfaces since this is the phase angle of the complex stress intensity factor. Thus, it is necessary and desirable to normalize  $K$  by a typical specimen dimension. Therefore, for simplicity and for both specimens A and B, we use reference length  $l = 1 \text{ mm}$ . The normalization must include this dimension, raised to the power  $i\epsilon$ . Usually the phase angle,  $\psi_2 - \psi_1$ , is small (see Eq. (2)). For example, if one compares specimens for which the reference length differs by a factor of 10, the change in phase angle is  $2.3\epsilon$ , that is,  $3.8^\circ$  for  $\epsilon = 0.028$  (the value for specimen

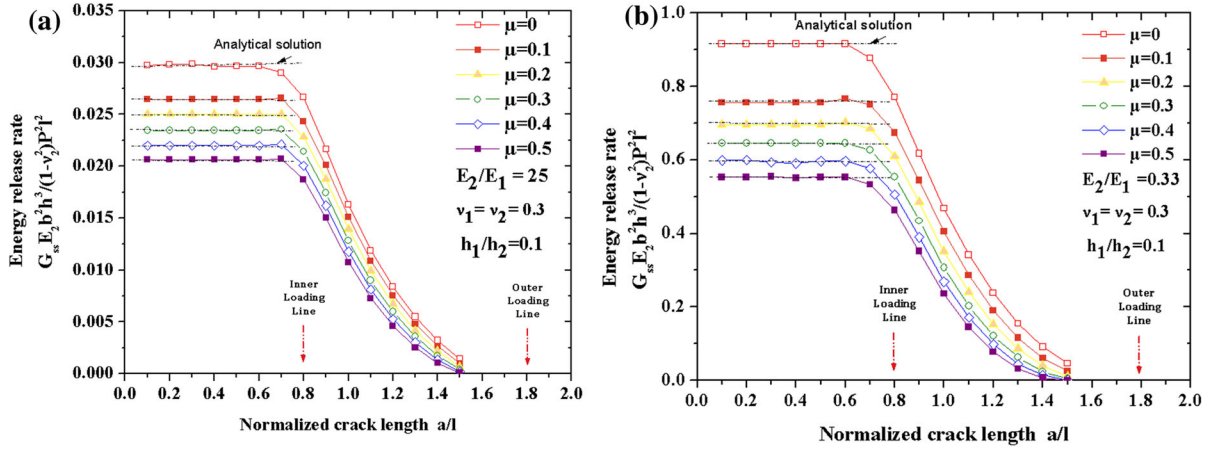


**Fig. 5** The trends in normalized energy release rate  $\mathcal{G}$  with relative crack length ( $a/l$ ) for various friction coefficients  $\mu$ . **a** These results were obtained for  $\eta = h_1/h_2 = 0.1$ ,  $\alpha = E_2/E_1 = 25$  and for  $\beta = \nu_1/\nu_2 = 1$  (Specimen B1). We note that, the comparison of the finite element results and the analytical solution

gave difference of less than 1%. **b** These results were obtained for  $\eta = h_1/h_2 = 0.1$ ,  $\alpha = E_2/E_1 = 0.33$  and for  $\beta = \nu_1/\nu_2 = 1$  (Specimen A1). We note that, the comparison of the finite element results and the analytical solution gave a difference of less than 1%

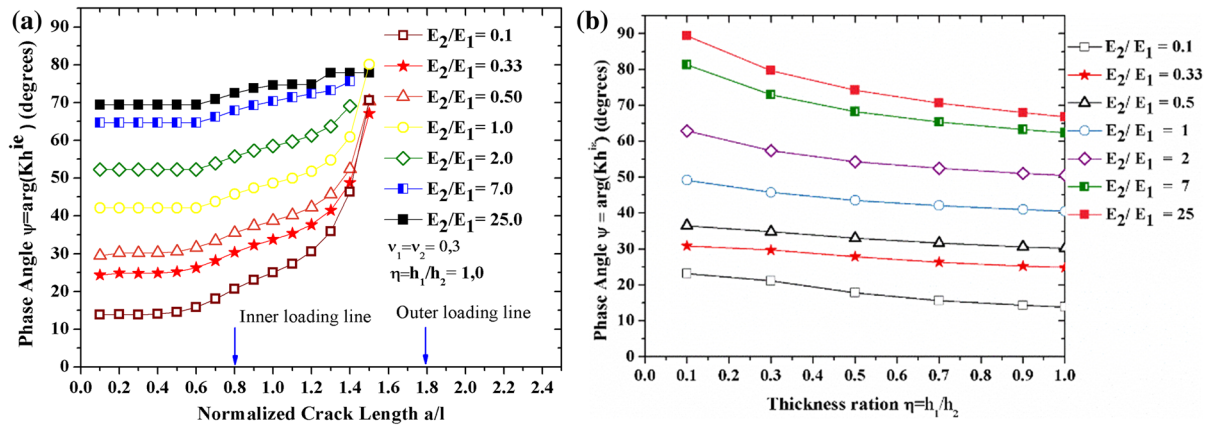


**Fig. 6** **a** The phase angle  $\psi$ , with respect to the crack length ratio  $a/l$  and modulus ratio  $\alpha = E_2/E_1$  for  $\eta = h_1/h_2 = 1$  and fixed Poisson's ratio  $\beta = \nu_1/\nu_2 = 1$ . **b** The phase angle  $\psi$ , with

respect to the thickness ratio  $\eta$  and modulus ratio  $\alpha = E_2/E_1$  for fixed Poisson's ratio  $\beta = \nu_1/\nu_2 = 1$

A in plane strain condition) and  $13.6^\circ$  for  $\epsilon = 0.1037$  (the value for specimen B in plane stress condition).

The general trends in normalized energy release rate  $\mathcal{G}$  with normalized crack length are shown in Fig. 5. As expected, the non-dimensional  $\mathcal{G}$  is seen to approach its steady-state value, when the crack propagates between the inner loading points. As the crack goes beyond the inner loading points, the Energy Release Rate decreases. The analytical solutions (4) and (7) for the steady-state values are plotted and compared with Finite Element Analysis. Within the steady-state region, the normalized Finite Element Energy

Release Rates  $\mathcal{G}$  are in good agreement with the analytical results. The maximum deviation is less than 1% (Fig. 5a, b).

The interfacial stress intensities factors (real and imaginary) and the associated phase angle are calculated using Finite Element Analysis and show the trends with relative thickness ratio  $\eta$  and relative crack length  $a/l$  (see Fig. 6a, b). The phase angle,  $\psi$ , is plotted vs. the normalized crack length in Fig. 7. The phase angle approaches a steady-state value for the same crack lengths as those exhibiting a steady-state energy release rate (Fig. 5). The friction has no effect on the phase

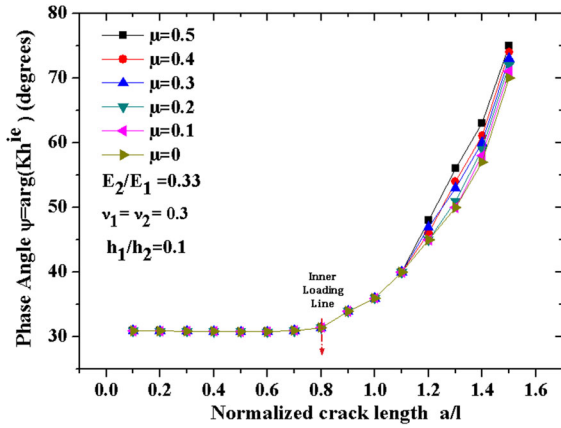


**Fig. 7** The trends in the phase angle  $\psi$ , with crack length for various friction coefficients for  $\alpha = 0.33$  for  $\eta = 0.1$  and fixed Poisson's ratio  $\beta = \nu_1/\nu_2 = 1$

angle in this zone. On the contrary, as the crack enters in the transient zone between the inner and outer loading lines, the phase angle becomes sensitive to crack length and increases substantially with increase of friction coefficient (see Fig. 7).

From Figs. 6 and 7, it can be seen that the phase angle  $\psi$  depends on relative layer thickness, relative elastic properties of the two materials, friction coefficients and the interfacial crack position beyond the inner loading line (transient zone). We attempt to explore the latter to increase range of the mode mixity. For this reason, the compliance method which is based on finite element analysis has been employed. In Fig. 8a, the calculated, normalized compliance of a sample geometry is plotted versus the normalized crack length for different friction coefficients. With knowledge of the experimental achieved compliance and assumed friction coefficient of each specimen configuration (see Table 4), the crack length can be determined (see Fig. 8a). Then, knowing the latter, the Energy Release Rate could be obtained (Fig. 8b). As expected, the energy release rate remains constant as long as the compliance increases linearly with increasing crack length and as soon as the compliance gradient decreases (see Fig. 8a), the Energy Release Rate in Fig. 8b decreases, and goes to zero.

### 3 Results and discussion

#### 3.1 Interfacial fracture patterns

Figure 9b shows the MEB observation around the interfacial crack propagation in the case of Aluminum

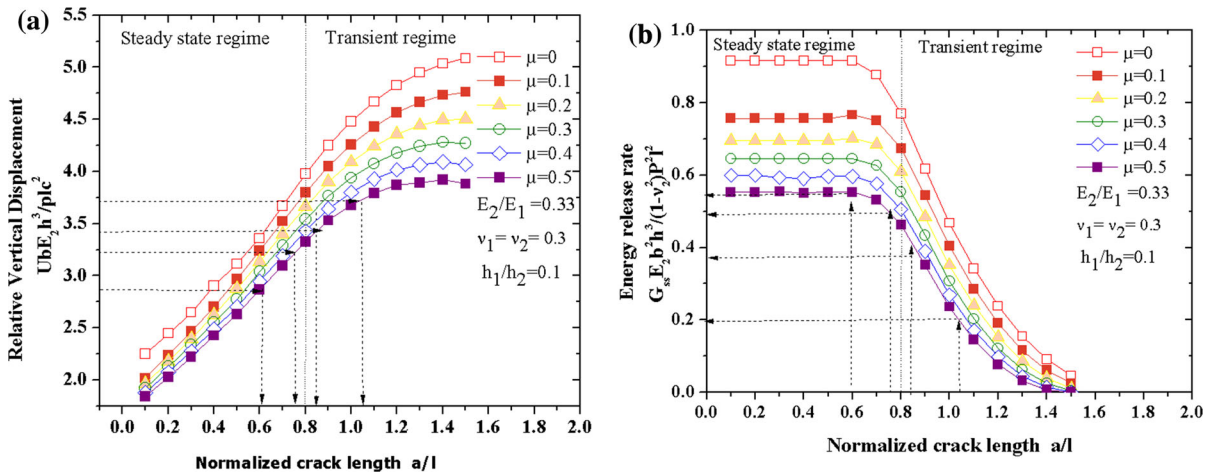
alloy (ASTM 2017)/stainless steel (ASTM 301) systems for loading phase angle  $\psi \sim 63^\circ$  (specimen A3). It shows that the crack surface is very rough and irregular ( $R_a = 2.87 \mu\text{m}$ ). The crack propagation occurs along the interface undulations between Aluminum alloy (ASTM 2017) and stainless steel (ASTM 301) and has network-like behavior shown by the attributes of mode II in homogenous materials. In the case of Aluminum alloy (ASTM 2017)/Epoxy/PMMA systems for loading phase angle  $\psi \sim 85^\circ$  (specimen B2), the interfacial crack runs along interface for a short distance ( $\sim 250 \mu\text{m}$ ), and then kinked to the other interface, leaving a portion of the epoxy layer. Such kinking is shown in Fig. 9c. For specimen A1, A2, the interfacial fracture is similar to cleavage fracture associated with mode I in homogenous materials. These observations agree with the characteristic mode mixity in the combined toughness plot, whereas the A1 and A2 specimens have low mode mixity and the A3, A4, B1 and B2 specimens have higher characteristic mode mixity.

#### 3.2 Interfacial toughness

For each specimen, the critical Energy Release Rate called interfacial toughness and the associated mode mixity  $\psi$  (based on reference length  $l = 1 \text{ mm}$ ) is determined by Finite Element results using the compliance method described above. The interfacial toughness  $\Gamma$  of specimen A ranges from  $111 \pm 12 \text{ Jm}^{-2}$  to  $413 \pm 22 \text{ Jm}^{-2}$ , whereas for specimens B, it varies from  $10.1 \pm 3 \text{ Jm}^{-2}$  to  $24.3 \pm 3 \text{ Jm}^{-2}$  (Fig. 10). We note that the characteristic mixed mode obtained covers a range: from about  $30^\circ$  to about  $73^\circ$  for specimen A and from about  $70^\circ$  to about  $85^\circ$  for specimen B. However, from our experimental results the interfacial toughness was found to have a strong phase angle dependence, i.e. it becomes larger with shear-mode loading and takes the form of a parabolic shape (see Fig. 10). The interfacial toughness,  $G_c$ , depends on many contributions: the intrinsic adhesive energy,  $\gamma_a$ , the rate of plastic dissipation near the crack front,  $\dot{W}_p$ , the rate of bulk viscoelastic dissipation,  $\dot{W}_v$ , and the shielding effect due to the initial roughness of the interface  $\Delta G_c$ . Therefore, the Energy Release Rate was expressed as:

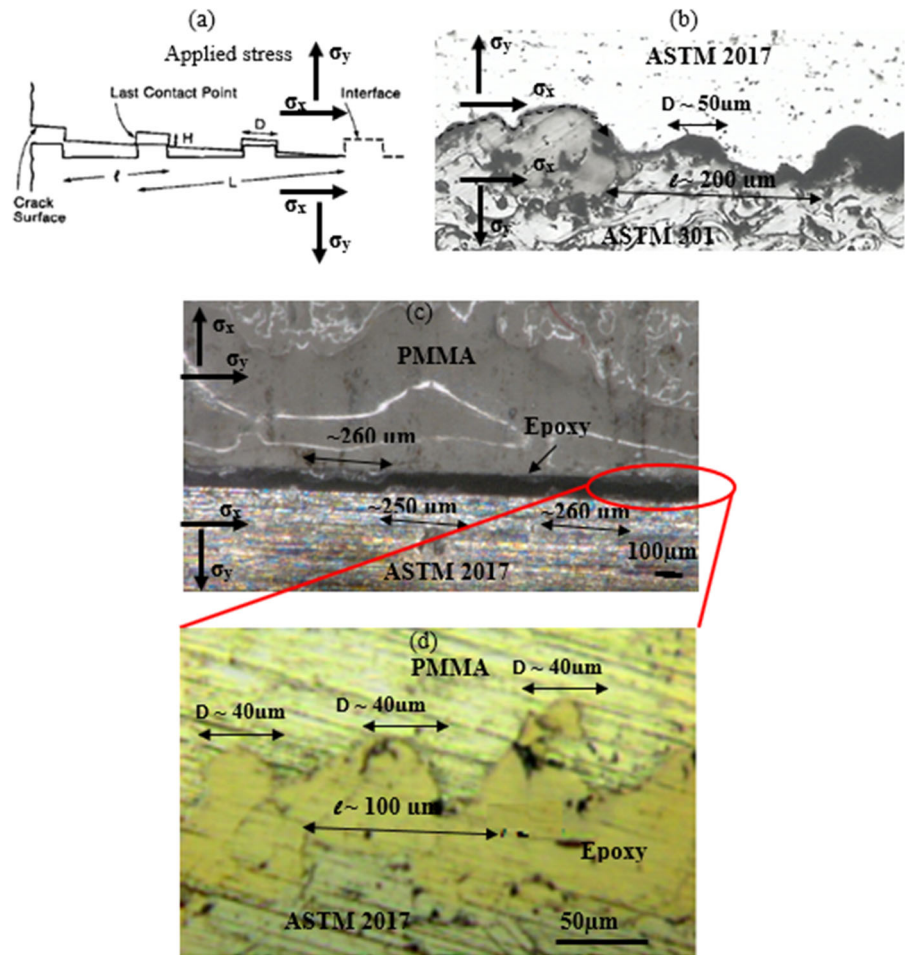
$$G_c = \gamma_a + \dot{W}_p + \dot{W}_v + \Delta G_c \quad (9)$$

Liechti and Chai (1992) calculated the  $\dot{W}_p$  and  $\dot{W}_v$  to explain the phase angle dependence of interfacial



**Fig. 8** a FEA of the normalized compliance to determine crack length, b FEA of the normalized energy release rate on crack length

**Fig. 9** a A schematic illustration of the zone model used to determine trends in  $G$  with phase angle of loading (Evans and Hutchinson 1989). b Non-planar Aluminum alloy (ASTM 2017)/stainless steel (ASTM 301) systems. Cracking occurs along the interface. c Aluminum alloy (ASTM 2017)/Epoxy/PMMA systems. The interface crack path abruptly changes from the upper interface (PMMA/Epoxy) to lower interface (ASTM2017/Epoxy). d Magnified view before crack delamination



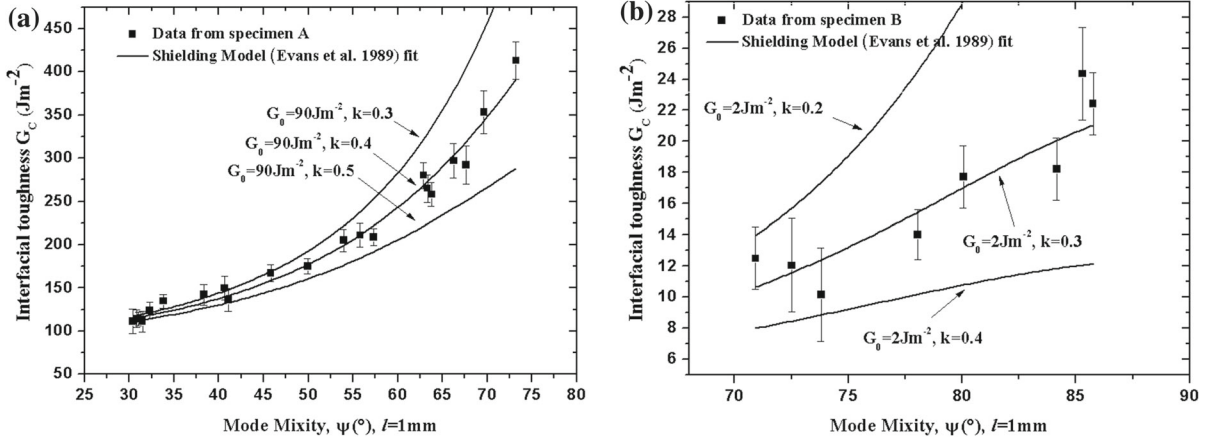


**Fig. 10** Interfacial toughness as function of the characteristic mixed mode. **a** The experimental data were fitted with  $G_0 = 90 \text{ J/m}^2$  and varied the  $k$  function to be 0.2, 0.3 and 0.4. **b** The

experimental data were fitted with  $G_0 = 2 \text{ J/m}^2$  and varied the  $k$  function to be 0.2, 0.3 and 0.4

fracture toughness for Epoxy–Glass material combination. They have found that their dependence of phase angle,  $\psi$ , is similar as the toughness values. However, the maximum value of both  $\dot{W}_p$  and  $\dot{W}_v$  were  $2.5 \text{ J/m}^2$  and  $3 \text{ J/m}^2$  respectively, more than the order of magnitude less than the maximum  $G_c$  value of  $36 \text{ J/m}^2$ . Here, we neglect the rate of plastic and the viscoelastic dissipations, even if they exist, and we address only the effect of the crack surface roughness for the interfacial fracture toughening. Therefore, the contact shielding model considered by [Evans and Hutchinson \(1989\)](#) was applied for our purpose. We also attempt to apply this model to an explanation for both Aluminum alloy (ASTM 2017)/stainless steel (ASTM 301) and Aluminum alloy (ASTM 2017)/Epoxy/PMMA systems.

The contacts resist the motion of the crack surface by means of friction and asperity locking on the surface, that resulted from crack growth along an initially rough interface and thereby modify the energy release rate or interfacial toughness at the crack front. The basic idea was that, under normal loading ( $\psi = 0^\circ$ ), the asperities would not touch and there would be no increase in  $G_c$ , all other dissipative effects being zero. Increasing amounts of shear loading ( $\psi > 0^\circ$ ), the asperities would contact and thus provide a shielding or toughening effect. A schematic illustration of the shielding model is shown in [Fig. 9](#). The Energy Release Rate including the contact shielding effect was expressed as follows:

$$G = G_0 \frac{1 + \tan^2 \psi}{1 + k^2(\lambda) \tan^2 \psi} \quad (10)$$

where  $G_0$  is the intrinsic interfacial energy release rate,  $k$  is a function of the ratio  $\lambda = D/l$ , which was given by [Budiansky et al. \(1988\)](#),  $l$  is the spacing between facet centers (microcrack), and  $D$  is the facet length shown in [Fig. 9](#). We varied the  $k$  function to be 0.2, 0.3 and 0.4 and assumed the intrinsic energy release rate  $G_0$  to be  $90 \text{ J/m}^2$ . The estimated results for various  $k$  are shown in [Fig. 10a](#). We try to repeat the same analysis on specimen B. We varied the  $k$  function to be 0.2, 0.3 and 0.4 and assumed the intrinsic energy release rate  $G_0$  to be  $2 \text{ J/m}^2$ . The function give us a best fit of  $k = 0.3$  ([Fig. 10b](#)).

With decreasing  $k$  value, which means that the crack surface roughness increases, the phase angle dependence of the energy release rate becomes larger. In the ASTM 2017/stainless steel (ASTM 301) systems, the facet spacing  $l$  could be taken to be about  $200 \mu\text{m}$  and the facet length  $D$  to be about  $50 \mu\text{m}$ , which could also be compared to the averaged values obtained from several SEM photographs ( $\lambda = D/l \sim 0.25$ ) ([Fig. 9b](#)). Thus, the  $k$  function in our case should be taken to be approximately 0.4. The same analysis was applied to the systems of Aluminum alloy (ASTM 2017)/Epoxy/PMMA except that here the kinking effect on interface crack was neglected. We consider the crack growth in one interface ([Fig. 9d](#)). The facet spacing  $l$  and the facet length  $D$  were measured  $100 \mu\text{m}$  and about  $40 \mu\text{m}$  respectively. This corre-

sponds to averaged values obtained from several SEM photographs ( $\lambda = D/l \sim 0.4$ ) (Fig. 9b). Thus, the  $k$  function should be taken to be approximately 0.34. Note, from this estimation, both energy release rates obtained in our experiment are very close to the results estimated by the contact shielding model.

## 4 Conclusion

The paper describes some extensions of the four-point bending tests for determining the toughness of interfaces, in both steady-state and transient regimes, as a function of mode mixity. Two sets of multi-material systems were studied: (i) Aluminum alloy (ASTM 2017)/epoxy/PMMA polymer and, (ii) Aluminum alloy (ASTM 2017)/stainless steel (ASTM 301) obtained by bonding and thermal spray respectively. Based on both numerical and experimental results obtained in this work, the following conclusions can be drawn:

1. To increase range of mode mixity ( $\psi$ ), the interfacial crack propagations beyond the central loading (transient régime) have been analysed. Besides, we have varied the relative elastic properties by reversing the notch position in multimaterial systems, and a relative layer thickness of multimaterial systems. These techniques allow us to characterize our studied systems: from about  $\psi \sim 30^\circ$  to  $73^\circ$  and  $\psi \sim 70^\circ$  to  $85^\circ$  for specimens A (ASTM 2017/stainless steel) and B (ASTM 2017/Epoxy/PMMA) respectively.
2. To determine the interfacial toughness  $G_c$  in transient regime, the compliance method has been used taking into consideration the friction coefficient between specimens and loading pins. As it was expected, the toughness curve followed the parabolic shape.
3. SEM observations were done after interfacial fracture tests. For Aluminum alloy (ASTM 2017)/stainless steel (ASTM 301) systems and for loading phase angle  $\psi \sim 63^\circ$ , we observe that the crack propagation occurs along the interface undulations between Aluminum alloy (ASTM 2017) and stainless steel (ASTM 301) and has network-like behavior that showed the attributes of mode II in homogenous materials. Whereas, for Aluminum alloy (ASTM 2017)/Epoxy/PMMA systems and for loading phase angle  $\psi \sim 85^\circ$ , the interfacial crack propagates along interface for a short distance ( $\sim 250 \mu\text{m}$ ), and then kinked to the other interface, leaving a portion of the epoxy layer.
4. The effects of non-planarity on the fracture resistance of interfaces have been investigated using a contact shielding model. The shielding model was applied to fit the interfacial toughness  $G_c(\psi)$ . The optimum parameter used were:  $G_0 = 90 \text{ J/m}^2$  and  $k = 0.4$ , and  $G_0 = 2 \text{ J/m}^2$  and  $k = 0.3$  for specimens A (aluminum alloys/stainless steel) and B (aluminum alloy/PMMA) respectively.

We believe that our proposed method named as the crack compliance method could serve as a useful benchmark method to estimate experimentally meaningful values of both interfacial fracture energy and stress intensities factors (real and imaginary) which are important fracture parameter. We note that in our study we have neglected the effect of plasticity, viscoelasticity dissipations and residual stresses. The latter are an important factor influencing the integrity and performance of multimaterials systems. The high residual stresses can lead to cracking, delamination of the coating, shape changes, etc., and in general, will weaken the performance and reliability of the entire part. Therefore, the works on the consequence of residual stresses on measuring the mixed mode cracking of bimaterials or multimaterials are in progress.

**Acknowledgements** The first author M.E.M. Zebar was supported by Algerian Ministry of Higher Education and Scientific Research (MESRS) under priority program. The authors would like to thank Lionel Auffray and Alban Aubertin for technical support. We also thank Svetlana Terekhina (ENSAM, LAMPA, Angers), for fruitful discussions and use of Abaqus license.

**Funding** The author(s) disclosed receipt of the following financial support for the research, authorship, and/or publication of this article: This study was supported by the French-Algerian collaboration project and financed by Algerian Ministry of Higher Education and Scientific Research (MESRS), Grant Number 595 PNE .

## Compliance with ethical standards

**Conflict of interest** The author(s) declared no potential conflict of interest with respect to the research, authorship, and/or publication of this article.

## References

- ABAQUS (2014) Abaqus 6.14 online documentation. Dassault Systèmes, Providence

- Becker TL Jr, McNaney JM, Cannon RM, Ritchie RO (1997) Limitations on the use of the mixed-mode delaminating beam test specimen: effects of the size of the region of  $K$ -dominance. *Mech Mater* 25(4):291–308
- Begley M, Hutchinson J (2017) *The mechanics and reliability of films, multilayers and coatings*. Cambridge University Press, Cambridge. <https://doi.org/10.1017/9781316443606>
- Budiansky B, Amazigo JC, Evans AG (1988) Small-scale crack bridging and the fracture toughness of particle-reinforced ceramics. *J Mech Phys Solids* 36:167
- Charalambides PG, Lund J, Evans AG, McMeeking RM (1989) A test specimen for determining fracture resistance of bimaterial interfaces. *J Appl Mech* 56:77–82
- Charalambides PG, Cao HC, Lund J, Evans AG (1990) Development of test method for measuring the mixed mode fracture resistance of bimaterial interface. *Mech Mater* 8:269–283
- Cherepanov GP (1979) *Mechanics of brittle fracture*. McGraw-Hill, New York
- Clarke DR, Levi CG (2003) Materials design for the next generation thermal barrier coatings. *Annu Rev Mater Res* 33(1):383–417
- Comte C, von Stebut J (2002) Microprobe-type measurement of Young's modulus and Poisson coefficient by means of depth sensing indentation and acoustic microscopy. *Surf Coat Technol* 154(1):42–48
- Dauskardt R, Lane M, Ma Q, Krishna N (1998) Adhesion and debonding dissimilar materials. *Eng Fract Mech* 59(6):725–735
- Dollhofer J, Beckert W, Lauke B, Schneider K (2000) Fracture mechanical characterisation of mixed-mode toughness of thermoplast/glass interfaces. *Comput Mater Sci* 19(1–4):223–228
- Evans AG, Hutchinson JW (1989) Effects of non-planarity on the mixed mode fracture resistance of bimaterial interfaces. *Acta Metall* 37(3):909–916
- Evans AG, Ruhle M, Dalgleish BJ, Charalambides PG (1990) The fracture energy of bimaterial interfaces. *Mater Sci Eng A* 126:53–64
- Gan Z, Mhaisalkar SG, Chen Z, Zhang S, Chen Z, Prasad K (2005) Study of interfacial adhesion energy of multilayered ULSI thin film structures using four-point bending test. *Surf Coat Technol* 198:85–89
- Harper CA (2002) *Handbook of plastics, elastomers, and composites*, 4th edn. McGraw-Hill, New York (ISBN: 9780071384766)
- Hattali ML, Valette S, Ropital F, Mesrati N, Tréheux D (2009) Study of SiC-nickel alloy bonding for high temperature applications. *J Eur Ceram Soc* 29:813–819
- Hattali ML, Valette S, Ropital F, Mesrati N, Tréheux D (2010) Calculation and experimental determinations of the residual stress distribution in alumina-Ni-alumina and alumina-Ni-nickel alloy systems. *J Mater Sci* 45:4133–4140. <https://doi.org/10.1007/s10853-010-4502-8>
- Hattali ML, Valette S, Ropital F, Mesrati N, Tréheux D (2012) Interfacial behavior on Al<sub>2</sub>O<sub>3</sub>/HAYNES®214™ joints fabricated by solid state bonding technique with Ni or Cu-Ni-Cu interlayers. *J Eur Ceram Soc* 32:2253–2265
- Hofinger I, Oechsner M, Bahr HA, Swain MV (1998) Modified four-point bending specimen for determining the interface fracture energy for thin, brittle layers. *Int J Fract* 92:213–220
- Hutchinson JW, Suo Z (1992) Mixed mode cracking in layered materials. *Adv Appl Mech* 29:63–89
- Ikeda T, Miyazaki N, Soda T (1998) Mixed mode fracture criterion of interface crack between dissimilar materials. *Eng Fract Mech* 59(6):725–735
- Liechti KM, Chai YS (1992) Asymmetric shielding in interfacial fracture under in-plane shear. *J Appl Mech* 59(2):295–304
- Matos PPL, McMeeking RM, Charalambides PG, Drory MD (1989) A method for calculating stress intensities in bimaterial interfaces. *Int J Fract* 40:235–254
- Odowd NP, Shih CE, Stout MG (1992) Test geometries for measuring interfacial fracture-toughness. *Int J Solids Struct* 29(5):571–589
- Ranjbar-Far M, Absi J, Mariaux G (2012) Finite element modeling of the different failure mechanisms of a plasma sprayed thermal barrier coatings system. *J Therm Spray Technol* 21(6):1234–44
- Rice JR (1988) Elastic fracture mechanics concepts for interfacial cracks. *ASME J Appl Mech* 55:98–103
- Rice JR, Sih GC (1965) Plane problems of cracks in dissimilar media. *ASME J Appl Mech* 32(2):418–423
- Rice JR, Suo Z, Wang J-S (1990) Mechanics and thermodynamics of brittle interfacial failure in bimaterial systems. In: Ruhle M et al (eds) *Acta-scripta metallurgica proceedings series*. Pergamon Press, London, pp 269–294
- Richards BT, Sehr S, De Francqueville F, Begley MR, Wadley HN (2016) Fracture mechanisms of ytterbium monosilicate environmental barrier coatings during cyclic thermal exposure. *Acta Mater* 103:448–60
- Sadki A, Hattali ML, Bradai MA, Younes R, Mesrati N (2016) Characterization and modeling of the mechanical behavior of aeronautical alloy based composite. *Univ J Chem* 4(1):10–19. <https://doi.org/10.13189/ujc.2016.040102>
- Suo ZG, Hutchinson JW (1990) Interface crack between 2 elastic layers. *Int J Fract* 43(1):1–18
- Swadener JG, Liechti KM, de Lozanne AL (1999) The intrinsic toughness and adhesion mechanisms of a glass/epoxy interface. *J Mech Phys Solids* 47(2):223–258
- Toya M (1992) On mode I and mode II energy release rates of interface crack. *Int J Fract* 56:345–352
- Wang J-S, Suo Z (1990) Experimental determination of interfacial toughness curves using Brazil-nut sandwiches. *Acta Mater* 38(7):1279–1290
- Wu C, Gowrishankar S, Huang R, Liechti KM (2016) On determining mixed-mode traction-separation relations for interfaces. *Int J Fract* 202(1):1–19
- Yang W, Sherman VR, Gludovatz B, Schaible E, Stewart P, Ritchie RO, Meyers MA (2015) On the tear resistance of skin. *Nat Commun* 6:6649
- Yuuki R, Liu J-Q, Xu J-Q, Ohira T, Ono T (1994) Mixed mode fracture criteria for an interface crack. *Eng Fract Mech* 47(3):367–377
- Zeng Z, Sakoda N, Tajiri T (2006) Corrosion behavior of wire-arc-sprayed stainless steel coating on mild steel. *J Therm Spray Technol* 15:431–437